Carbon 159 (2020) 149–160

Contents lists available at ScienceDirect

Carbon

journal homepage: www.elsevier.com/locate/carbon

# Electrochemical generation of $Fe_3C$/N-doped graphitic carbon nanozyme for efficient wound healing *in vivo*

Yang Li [a, b, 1], Weishuai Ma [a, b, 1], Jing Sun [c], Min Lin [c], Yusheng Niu [d], Xuecheng Yang [a], Yuanhong Xu [a, b, *]

[a] Department of Urology, Key Laboratory of Urinary System Diseases, The Affiliated Hospital of Qingdao University, Qingdao, 266003, China
[b] College of Life Sciences, College of Materials Science and Engineering, Qingdao University, Qingdao, 266071, China
[c] College of Polymer Science and Engineering, Qingdao University of Science & Technology, Qingdao, 266071, China
[d] School of Tourism and Geography Science, Qingdao University, Qingdao, 266071, China

ARTICLE INFO

*Article history:*
Received 26 September 2019
Received in revised form
18 November 2019
Accepted 30 November 2019
Available online 2 December 2019

ABSTRACT

The emergence of antibiotic resistance has been advancing the exploration of highly-efficient, cost-effective and biocompatible enzymatic nanomaterials (i.e. nanozyme) as antibacterial agents. Iron carbide ($Fe_3C$) based nanomaterials were suggested to be promising catalysts as well as nanozymes, but were limited with the low enzyme-like activity and the high temperature-carbonization, time-consumption preparation process. Herein, one efficient peroxidase-like $Fe_3C$/N-doped graphitic carbon nanomaterial ($Fe_3C$/N–C) was prepared through a one-step mild electrochemical method. Therein, the $FeSO_4$/histidine (His) mixture and graphite rod were used as the electrolyte and the electrode, respectively. The generation of $Fe_3C$/N–C was coincidentally benefiting from the specific affinity interactions between the His derived carbon nanodots (CNDs) and the iron ion. The $Fe_3C$/N–C nanozyme could enable the decomposition of hydrogen peroxide ($H_2O_2$) to hydroxyl radical (•OH), resulting in higher broad-spectrum antimicrobial activity than $H_2O_2$ alone. Accordingly, high concentration of $H_2O_2$ can be avoided in bacterial infection, but accelerated wound healing *in vivo* can be achieved simultaneously. The superior peroxidase-like ability can be attributed to the intrinsic active sites in the $Fe_3C$ while using the carbon nanosheets as the matrix. And the synergistic interface effect between $Fe_3C$ and N-doped graphite carbon could lead to the enhancement of peroxidase mimicking activity in return.



## 1. Introduction

The emergence of antibiotic resistance has prompted the development of new drugs and materials to combat pathogenic microorganisms [1]. Recently, because of their unique chemical and physical properties, nanomaterials have been regarding as the promising alternatives for improving disinfection treatment system [2,3]. In particular, the nano-materials with biomimetic enzymatic properties (i.e. nanozymes) were suggested to be efficient in assisting the antibacterial activity of $H_2O_2$ [4,5]. For example, the peroxidase-mimic behaviour of the gold or platinum nanomaterials could decompose $H_2O_2$ into more highly oxidative hydroxyl radical (•OH) to achieve the purpose of sterilization [6,7]. Accordingly, lower concentration of $H_2O_2$ was needed in the presence of the nanozyme to reach the comparative antibacterial efficacy of the $H_2O_2$ alone [8,9]. Meanwhile, it can avoid healthy tissues damage and slow healing wounds resulting from the too-high concentration $H_2O_2$. Despite the achievements, it is still a significant challenge to develop an ideal nanozyme fulfilling the requirements of excellent biocompatibility, high catalytic activity and cost-effectiveness simultaneously.

Iron carbide ($Fe_3C$), one of the transition metal carbides, processed excellent thermal stability, superior mechanical strength, environmental friendliness and excellent catalytic activity [10,11]. Besides, the carbon matrix for $Fe_3C$ nanoparticles encapsulation could improve their electronic conductivity and chemical stability [10]. Previous researches have shown that doping heteroatoms into the carbon matrices could further enhance the catalytic activity of the $Fe_3C$ [12,13]. Accordingly, the $Fe_3C$-based materials have been

* Corresponding author. Department of Urology, Key Laboratory of Urinary System Diseases, The Affiliated Hospital of Qingdao University, Qingdao, 266003, China.
*E-mail addresses:* yhxu@qdu.edu.cn, yuanhong.xu@yahoo.com (Y. Xu).
[1] Contributed equally to this work.

https://doi.org/10.1016/j.carbon.2019.11.093
0008-6223/

begun to attract considerable interest recently not only in the fields of electro-catalytic process [10,14], dye-sensitized solar cells [15], electro-magnetic wave absorbing [16], superior supercapacitors [17], but also in the field of nanozyme catalysis [11,18]. However, the $Fe_3C$-based nanozyme catalytic applications were fewer than expected, which should be resulted from the high-temperature carbonization treatment and time-consumption complex process to prepare the $Fe_3C$ as well as the corresponding matrices [19–22]. Thus, it is necessary to develop a facile and low energy-consumption strategy to fabricate the enzyme-like $Fe_3C$-based nanomaterials.

Previous reports indicated that the carbon materials with ample oxygen-containing groups, especially CNDs have specific affinity interactions with the iron ion ($Fe^{2+}$/$Fe^{3+}$) to form coordination complexes of Fe-CNDs. The specific interaction was usually applied for specific iron ion assays [23–25]. Also, the CNDs can be prepared by the bottom-up electrochemical (EC) oxidation using the small organic molecules such as amino acids as the precursors [25]. Meanwhile, the EC exfoliation of the graphite rod can result in graphene matrics, and especially the electrolyte, can be chosen to dope the exfoliated graphene materials as well [26–28]. It is reported that there is a sharp interaction between Fe (III) and CNDs, which can coordinate the formation of complexes [29]. However, what changes will happen to $Fe^{2+}$/$Fe^{3+}$-His complexes and $Fe^{2+}$/$Fe^{3+}$-CNDs stimulated by EC are not yet studied. Inspired by these interesting phenomena, the preparation of $Fe_3C$-based materials was designed to be conducted by the EC exfoliation of the graphite rod using $FeSO_4$ and L-histidine as the electrolyte. Excitingly, $Fe_3C$/N-doped graphitic carbon nanomaterials ($Fe_3C$/N–C) could be obtained, which possesses excellent peroxidase mimicking activity toward $H_2O_2$ in the presence of TMB. Based on the characterization results such as the high-resolution transmission electron microscope (HRTEM), X-ray photoelectron spectroscopy (XPS), X-ray diffraction (XRD) patterns, we analyzed the formation mechanism of $Fe_3C$/N–C. In addition, the efficiency and applicability of the as-prepared $Fe_3C$/N–C based antibacterial system have been verified to the healing treatment of bacterial-infection wounds in mice.

## 2. Experimental section

### 2.1. Chemicals and instruments

Iron (II) sulfate heptahydrate ($FeSO_4 \cdot 7H_2O$, Mol. Wt. 278.02, purity 99.0%), Iron (III) sulfate hydrate ($Fe_2(SO_4)_3 \cdot xH_2O$, Mol. Wt. 399.88), hydrogen peroxide 30% aqueous solution ($H_2O_2$, Mol. Wt. 34.01, purity ≥30.0%) and ethanol ($C_2H_4OH$, Mol. Wt. 46.07, purity 99.7%) were provided by Sinopharm chemical reagent Co., Ltd., China. L-Histidine (His, Mol. Wt. 155.15, purity 99%), L-cysteine (Cys, Mol. Wt. 121.16, purity 99%), L-aspartic acid (Asp, Mol. Wt. 133.10, purity 99%), L-serine (Ser, Mol. Wt. 105.09, purity 99%), L-methionine (Met, Mol. Wt. 149.21, purity 99%), L-arginine (Arg, Mol. Wt. 174.2, purity 99%), 3, 3′, 5, 5′-Tetramethylbenzidine (TMB, Mol. Wt. 240.34, purity 98%), peroxidase horseradish (POD, > 250 U/mg), 3-(4, 5-dimethyl-2-thiazolyl)-2, 5-diphenyltetrazolium bromide (MTT, Mol. Wt. 414.32, purity 98%), 4′-6-diamidino-2-phenylindole (DAPI), propidium iodide (PI), terephthalic acid (TA, Mol. Wt. 166.13, purity 99%). Lysogeny broth (LB) medium, Dulbecco's modified Eagle's medium (DMEM). Deionized distilled water was applied in the experiment. All the experiments involving animals were approved by the Institutional Animal Care and Use Committee (IACUC) at Qingdao University.

The morphology of $Fe_3C$/N–C nanomaterials was observed on a JEOL Ltd JEM-2010 transmission electron microscope (JEOL Ltd., Japan). The PL spectra were performed on an Edinburgh instruments spectrofluorometer FS5 (Edinburgh, U. K.) with the excitation/emission slits of 5.0 nm × 5.0 nm. The ultraviolet–visible (UV–Vis) absorbance was gained from a Mapada UV-6300 double beam spectrophotometer (Shanghai, China). The Raman spectra were carried out on a DXR2 micro Raman imaging spectrometer (Thermo Fisher, U.S). FTIR was performed on a Nicolet 5700 FTIR spectrometer (Thermo Electron Scientific Instruments Corp., USA). The XPS data were collected on an ESCALab220i-XL electron spectrometer (VG Scientific, West Sussex, U. K.) using 300 W Al Kα radiation. The XRD was recorded on a Rigaku D-MAX 2500/PC with the Cu K α radiation (λ = 1.54056 Å) (Tokyo, Japan).

### 2.2. Synthesis of the $Fe_3C$/N–C

$Fe_3C$/N–C was generated through a facile electrochemical method. Typically, the electrolyte solution was composed of $FeSO_4$ (0.1 M) and L-histidine (His, 0.02 M) at room temperature (25 °C). Then, Pt sheets (area >1.0 $cm^2$) and graphite rod were used as the cathode and the anode, respectively. The electrolysis reaction was conducted at a voltage of 5 V with stirring at 500 rpm for 8 h. Then the resulted reaction mixture was under ultrasound treatment at 200 W for 90 min, being followed with centrifugation at 10,000 rpm for 10 min to obtain grey-black precipitates. The precipitate was treated with washing and freeze-drying to reach the final product. Control experiments were conducted as follows: **1**, the anode electrode was replaced by Pt electrode (control **1**); **2**, the electrolyte composition was replaced by pure $FeSO_4 \cdot 7H_2O$ solution (control **2**); **3**, the electrolyte composition was replaced by mixture of $Fe_2(SO_4)_3 \cdot xH_2O$ and His (pH = 2.14), the anode electrode was replaced by Pt electrode (control **3**); **4**, the electrolyte composition was replaced by histidine solution with sulfuric acid adjusting pH = 5.69 and the anode electrode was replaced by Pt electrode (control **4**); **5**, the electrolyte is $FeSO_4 \cdot 7H_2O$ and His solution with sulfuric acid adjusting pH = 2.14 (control **5**); **6**, the electrolyte composition was replaced by ultrapure water with sulfuric acid adjusting pH = 5.69 (control **6**); **7**, the electrolyte composition was replaced by histidine solution with sulfuric acid adjusting pH = 5.69 (control **7**). The other operating conditions were kept unchanged for the control experiments.

### 2.3. Measurements of the peroxidase-like activity and the kinetic parameters of the as-obtained $Fe_3C$/N–C

The oxidation of TMB by $Fe_3C$/N–C/$H_2O_2$ in NaAc-HAc buffer (pH = 4.0) were studied. The absorbance peaks at 652 nm was recorded. The reactions were performed in 1 mL acetate buffer solution at pH 4.0, containing $Fe_3C$/N–C (50 μg $mL^{-1}$), $H_2O_2$ (100 μM) and TMB (1 mM). The other groups including TMB + $H_2O_2$, $Fe_3C$/N–C + TMB, $Fe_3C$/N–C + $H_2O_2$, control 1 + TMB + $H_2O_2$, control 6 + TMB + $H_2O_2$, control 7 + TMB + $H_2O_2$ were selected as the controls. After 5 min reaction, $Fe_3C$/N–C was centrifuged to terminate the colorimetric reaction. Photos of the reaction solutions were collected, and the corresponding UV–vis absorbance was determined with a UV-6300 double beam spectrophotometer (Shanghai, China). The pH or temperature tolerance of the $Fe_3C$/N–C was studied with various pH of 1.0–12.0 at 25 °C for 5 min or in acetate buffers with the pH 4.0 at the different temperature from 25 to 70 °C for 5 min. Then the solution was cooled in the ice bath, and its relative activity was determined. The maximum activity of each group was defined as a relative value of 100%. The kinetics was performed by monitoring the absorbance variation at 652 nm. The tested samples were $Fe_3C$/N–C (50 μg $mL^{-1}$) mixed with different concentration of $H_2O_2$ and TMB in the acetate buffer (pH = 4.0). The Michaelis–Menten equation$V = V_{max} \times [S]/(K_m + [S])$ was applied to calculate the apparent kinetic parameters. Information in detail can be found in Section S1

in the Supporting Information.

### 2.4. Measurement of the •OH

TA was applied as the fluorescent probe for tracking the •OH, which was non-fluorescent itself but can react with •OH to produce the highly fluorescent product, 2-hydroxy terephthalic acid (TAOH). The reactions were performed in the phosphate buffer saline (PBS) buffer solution (0.2 M, pH = 7.4), including $Fe_3C$/N–C (100 μg $ml^{-1}$), TA (0.5 mM), $H_2O_2$ (1.0 mM). After 12 h of reaction, the fluorescence measurements of the samples were performed on the spectrofluorometer FS5 (Edinburgh, U·K.).

Electron spin resonance spectroscopy (ESR) measurements were conducted on a standard X-band Bruker E–500 EPR spectrometer (Karlsruhe, Germany) at ambient temperature. The spin trap, 5,5-dimethyl-1-pyrroline N-oxide (DMPO), was applied to identify the •OH generated from $H_2O_2$ decomposition in the presence of peroxidase-like $Fe_3C$/N–C. 50 mL of the control or sample solutions with $H_2O_2$ (10 mM), $Fe_3C$/N–C (20 μg $mL^{-1}$) and DMPO (0.04 M) were put in the capillary glass tubes and being sealed. The ESR spectra were collected 10 min after initiating the •OH generation. All the above operations were performed in the deoxidized acetate buffer (200 mM, pH 4.0). Instrument settings of 1 G field modulation, 100 G scan range, and 20 mW microwave power were used to detect the spin adducts.

### 2.5. Bacterial culture and antibacterial experiments

*Staphylococcus aureus (S. aureus)* and *Escherichia coli (E. coli)* were inoculated into 50 mL LB medium and incubated under the condition of 37 °C for 12 h under 180 rev $min^{-1}$. After that, the bacteria were diluted to $10^6$ CFU $mL^{-1}$. The as-prepared bacterial solution (200 μL) was mixed with $Fe_3C$/N–C (100 μg $mL^{-1}$) and $H_2O_2$ (1.0 mM) at 37 °C for 30 min. After treatment, the mixture was cultured on a solid medium under the condition of 37 °C for 24 h based on the colony-forming units (CFU) method. Control experiments those without $Fe_3C$/N–C or $H_2O_2$ were also conducted. Both the live/dead fluorescent staining and SEM has been performed to identify the live and dead *E. coli* cells, the information in detail can be found in S2 and S3 of the Supporting Information.

### 2.6. Mouse injury model and histology

To assay the antibacterial properties of $Fe_3C$/N–C *in vivo*, a mouse wound model was developed. The four groups of 12 male Sprague - Dawley (SD) rats with about 1 $cm^2$ wound area (6 weeks, 200 g, and three rats per group) were randomly divided into four groups, which will be treated with PBS, $H_2O_2$ (1 mM), $Fe_3C$/N–C (100 μg $mL^{-1}$) and $H_2O_2$ + $Fe_3C$/N–C, respectively. The rats were injected with $1 \times 10^6$ of *S. aureus* on their wound. The wound healing would be observed every two days for the next six days. Then the rats were sacrificed on the sixth day, and the wound tissues were harvested. To calculate the number of bacteria in each group, the tissues of wound were kept in PBS buffer at 37 °C overnight. The solutions were then diluted, and the amount of the bacteria were quantified by the CFU method.

After the sixth day of the experiment, the wound tissues in different groups were harvested and fixed in 4% paraformaldehyde solution. Then the tissue samples were processed routinely into paraffin, and the sections were stained with hematoxylin and eosin (H&E) for histological analysis.

### 2.7. MTT assays and in vivo biosafety of the $Fe_3C$/N–C

The MTT assays were performed to confirm the dependence of the viability of the HeLa cells on the $Fe_3C$/N–C doses (See S4 in the Supporting Information). To evaluate the biosafety of $Fe_3C$/N–C *in vivo*, the as-prepared $Fe_3C$/N–C at different concentrations including 100 and 200 μg $mL^{-1}$ was injected intravenously into the rats, respectively [30]. The control group was treated with PBS buffer. After six-day treatment, significant organs including heart, liver, spleen, lung, and kidney were collected for pathological examination. Besides, the blood samples were also harvested for physiological index examination.

## 3. Results and discussion

### 3.1. Preparation and characterization of the $Fe_3C$/N–C

As shown in Scheme 1, the nanozyme herein was synthesized via the electrochemical preparation strategy using the mixture of $FeSO_4 \cdot 7H_2O$ and His as the electrolyte. The graphite rod and Pt sheet were applied as the anode and cathode, respectively. The colour of the electrolyte firstly varied from yellow-green to orange in 30 min. With the ongoing time, it turned to brown and then to dark finally (Fig. S1). The precipitates were then collected after the ultrasound, washing and freeze-drying treatment, respectively.

The morphology of the products was characterized by TEM (Fig. 1A–B), showing nanodots with average diameters of 5 nm, uniformly dispersing on the nanosheets. The high-resolution TEM (HRTEM) images reveal that the as-obtained products have a well-defined crystalline with lattice spacing at 2.5 Å corresponding to the (020) plane of $Fe_3C$ (JCPDS: 03–0411) (the yellow circle in Fig. 1C) [31,32]. Also, a lattice distance of 3.4 Å of the nanosheets, being ascribed to the (002) lattice fringe of graphite-2H (JCPDS: 41–1487). The three grey-black regions a, b, and c marked with green arrows in Fig. 1C have the same lattice fringes of graphite-2H, confirming the dispersion of CNDs on the graphite sheets. The HAADF-STEM image (Fig. 1D) shows that the even distribution of the Fe, C and N elements in the graphite-2H nanosheets. These results showed that the as-prepared products should be due to the $Fe_3C$ nanomaterials dispersed on the N-doped graphitic carbon matrix (named as $Fe_3C$/N–C).

To further confirm the crystalline feature of the as-obtained products, X-ray diffraction (XRD) patterns of $Fe_3C$/N–C and other products of the three control groups were shown in Fig. 2A. The XRD pattern of $Fe_3C$/N–C (line a in Fig. 2A) shows peaks at 26.38°, 42.22°, 44.39°, 54.54°, 77.24° and 83.18° could be assigned to the crystal planes of (002), (100), (101), (004), (110) and (112) of

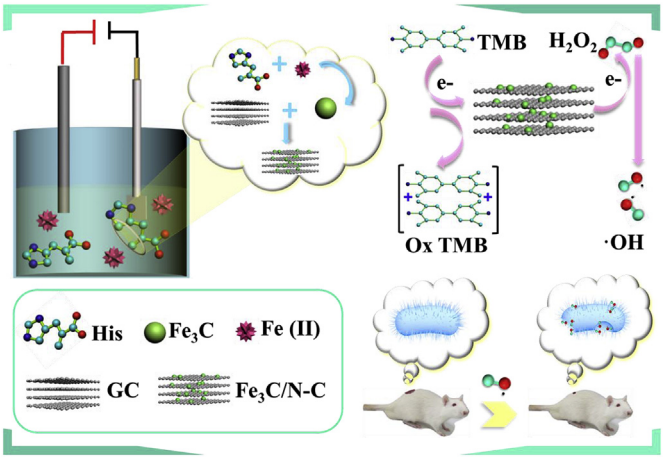


**Scheme 1.** Schematic illustration for the synthesis of the $Fe_3C$/N–C as well as the $Fe_3C$/N–C used in the wound disinfection *in vivo*.

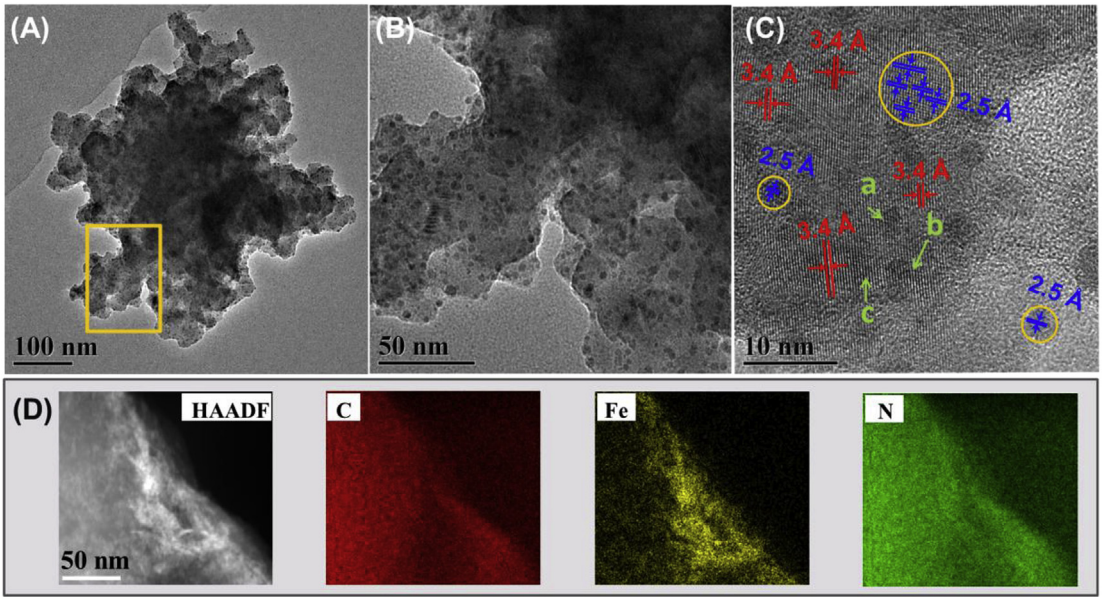


**Fig. 1.** Morphology characterization of the $Fe_3C$/N–C: (A) TEM image. (B) Enlarged view of (A). (C) HRTEM. (D) STEM and corresponding elemental mapping images. (A colour version of this figure can be viewed online.)

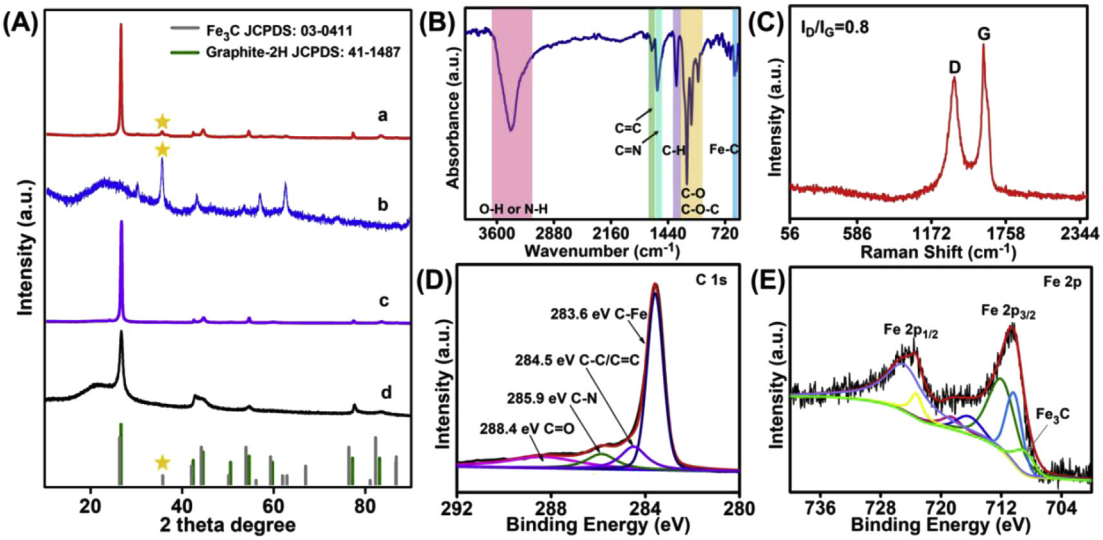


**Fig. 2.** (A) XRD patterns of the as-obtained products under different synthetic conditions: a: mixture of $FeSO_4 \cdot 7H_2O$ and His as the electrolyte, C rod as anode; b: control **1**; c: control **2**; d: control **3**. (B) and (C) are FTIR and Raman spectra of the $Fe_3C$/N–C, respectively. High-resolution XPS spectra of (D) C 1s and (E) Fe 2p of the $Fe_3C$/N–C, respectively. (A colour version of this figure can be viewed online.)

graphite-2H (JCPDS: 41–1487), respectively. And then the diffraction peaks at 42.22°, 44.39°, 77.24° and 83.18° can also be attributed to the crystal faces of (200), (013), (115) and (322) of $Fe_3C$ (JCPDS: 03–0411), respectively [33]. The weak peak at 35.89° should be ascribed to the (020) crystal plane of $Fe_3C$ (JCPDS: 03–0411). That the intensity of the diffraction peaks for the graphitic-2H is much stronger than those of the $Fe_3C$ suggested the high degree of the graphitization in the as-prepared $Fe_3C$/N–C. To confirm the carbon source of the $Fe_3C$ was from the His not from the graphite rod, we replaced graphite rod with Pt electrode while keeping a mixture of $FeSO_4 \cdot 7H_2O$ and His as the electrolyte. As shown in the line b of the XRD pattern (Fig. 2A), there was still existing the sharp diffraction peak at 35.89° corresponding to the (020) crystal plane of $Fe_3C$. Accordingly, it can be concluded that the carbon source in $Fe_3C$ was originated from His. Line c in Fig. 2A represents the XRD of the control product prepared by simple $FeSO_4$ solution as the electrolyte. The positions of the peak are only consistent with graphite-2H, and there is no crystallization peak of $Fe_3C$. Thus, it can be concluded that the existence of His was a requisite for the formation of $Fe_3C$. Since the ferrous iron ($Fe^{2+}$) is easily oxidized to trivalent iron ($Fe^{3+}$), $Fe_2(SO_4)_3 \cdot xH_2O$ was also tested to replace the $FeSO_4 \cdot 7H_2O$. Accordingly, no typical peak of $Fe_3C$ was observed in the corresponding XRD (curve d in Fig. 2A). It indicated that the oxidation of $Fe^{2+}$ played a crucial role in the generation of $Fe_3C$. Through a series of control experiments, $Fe^{2+}$ and His were confirmed to be the prerequisites for the preparation of $Fe_3C$.

Based on the characterizations and control experiments above, the formation mechanism of $Fe_3C$/N–C was supposed mainly

through the following processes: N-doped CNDs (N-CNDs) could be generated via the bottom-up electrochemical (EC) oxidation of the His. The oxidation process would transform most $Fe^{2+}$ to $Fe^{3+}$. Meanwhile, the medium complex between the His and $Fe^{3+}/Fe^{2+}$ or between the N-CNDs and $Fe^{3+}/Fe^{2+}$ could be formed. The further electrolysis would lead to the carbonization of the complex to $Fe_3C$. At the same time, the graphite rod can be peeled off to graphite-2H nanosheets under electrochemical exfoliation, which then captures the $Fe_3C$ particles and remaining N-CNDs to form $Fe_3C$/N–C.

Generally, the N-CNDs can be obtained by bottom-up electrochemical method via electro-oxidation, electro-polymerization, carbonization and passivation of the amino acids [25,34]. It confirmed that during the electro-oxidation of amino acids, the adsorbed intermediates were either hydrolyzed to formaldehyde and ammonia by anode [35] or oxidized to carbon ions. Carbon ions were also subsequently hydrolyzed to formaldehyde and ammonia in the solution. It was speculated that His was also under the electro-oxidation process, since the His was a basic amino acid (pKa 7.59), the product should be formaldehyde and ammonium ion ($NH_4^+$) in the medium of pH 5.69. The main electro-oxidation and electro-polymerization process are as follows:

$$C_4H_5N_2CH(NH_3^+)COOH \rightarrow C_4H_5N_2CH(NH_3^+)COO(M)+H^+ + e^- \quad (1)$$

$$C_4H_5N_2CH(NH_3^+)COO(M) \rightarrow (NH_3^+)CHC_4H_5N_2(M)+CO_2 \quad (2)$$

$$(NH_3^+)CHC_4H_5N_2(M)+H_2O \rightarrow NH_4^+ + RCHO + H^+ + e^- \quad (3)$$

Upon the applied voltage of 5 V, the electro-oxidation of His occurred to form $(NH_3^+)CHC_4H_5N_2(M)$, which subsequently reacted with the un-oxidized His molecules via the amidation reaction to produce $C_4H_5N_2CH(NH_2)CONHCHC_4H_5N_2^+$ ions. Then it could further result in the formation of N-CNDs via the carbonization and passivation process [24,25,34].

As measured, the pH is 5.69 for the mixture of $Fe^{2+}$ and His while 2.14 for that of $Fe^{3+}$ and His, respectively. That is to say, the hydrolysis of $Fe^{2+}$ provided mild acid conditions for the subsequent electrochemical generation of N-CNDs from His. While too acidic or basic conditions should not be favorable for the N-CNDs generation via inhibiting the process (1) or accelerating the process (3) accordingly, while this weakly acidic condition is just conducive to the formation of N-CNDs from basic AAs. As shown, nanodots at about 4–5 nm in size can be observed by TEM (Fig. S2) for the product prepared by adjusting the pH of His electrolyte to 5.69 using $H_2SO_4$ rather $FeSO_4$ (control **4**). Besides, the corresponding XRD spectrum (curve a in Fig. S3) showed carbon diffraction peak, confirming the possible formation of N-CNDs at this mild acidic condition (pH 5.69). In addition, a control experiment was also carried out when the pH of His and $FeSO_4$ solution was adjusted to 2.14 (control **5**), which mimics the pH of $Fe^{3+}$ and His mixture solution and also inhibits the oxidation of $Fe^{2+}$ to $Fe^{3+}$. The XRD of the as-controlled product (curve b in Fig. S3) shows a similar diffraction peak for $Fe_3C$-poor/N–C as that of the curve a in Fig. 2A, and relatively weaker diffraction peak at 35.89° for $Fe_3C$. Meanwhile, the high-resolution XPS showed that the C 1s spectrum (Fig. S4A) is the same as in Fig. 2D, while the integral area 64% of C–Fe in C 1s spectrum (Fig. S4A) is smaller than that of 66% in Fig. 2D. The $Fe_3C$ peak in the Fe 2p spectrum (Fig. S4B) also showed a similar changing trend. These results confirmed that the too acidic background solution such as the mixture of His and $Fe^{3+}$ was not favorable for the formation of $Fe_3C$/N–C. Also, it showed that the electrochemical oxidation played the determining role while the oxidation process of $Fe^{2+}$ to $Fe^{3+}$ played promoting one in the formation of $Fe_3C$. Photoluminescence (PL) quenching via the iron ion of the as-prepared N-CNDs synthesized by control experiment **4** was also carried out. As shown in Fig. S5, the PL quenching of N-CNDs by $Fe^{3+}$ was 45%, while that of N-CNDs by $Fe^{2+}$ was 30%. It indicates that the complexation between $Fe^{3+}$ and N-CNDs is much stronger and thus more conducive to the formation of $Fe_3C$. Meanwhile, graphite-2H sheets formed by electrochemical stripping of graphite rods could not only act as the supporting carrier preventing the aggregation of $Fe_3C$, but also improve the electronic transmission ability of $Fe_3C$.

As control, other amino acids (AAs) such as L-cysteine (Cys, $C_3H_7NO_2S$), L-methionine (Met, $C_5H_{11}NO_2S$), L-aspartic acid (Asp, $C_4H_7NO_4$), L-serine (Ser, $C_3H_7NO_3$), glycine (Gly, $C_2H_5NO_2$) and L-arginine (Arg, $C_6H_{14}N_4O_2$) were tested as the precursors for the CNDs synthesis by bottom-up electrochemical method [25]. Therein, the AAs such as Cys (pKa = 5.05), Met (pKa = 5.74), Asp (pKa = 2.77), Ser (pKa = 5.68) and Gly (pKa = 5.97) were all acidic amino acids, which needed alkaline conditions to form the CNDs during the electrochemical oxidation process [25,36]. Since the pH of the mixture of these acid AAs and $FeSO_4$ is about 3–4, so the acid conditions are not suitable for the CNDs generation from these acid AAs using the electrochemical method. Arg is with the isoelectric point (pKa) of 10.76, belongs to one basic amino acid. But the mixture of Arg and $FeSO_4$ is 7.16, which is not favorable for the N-CNDs formation from Arg since it also needs mild acid condition. As indicated in the TEM characterization, the electrochemical oxidation using Asp + $FeSO_4$, Ser + $FeSO_4$ or Arg + $FeSO_4$ as electrolytes wouldn't result in CNDs (Fig. S6). Therefore, His is further confirmed to be more suitable precursor for the CNDs generation in this case and subsequently for the formation of the $Fe_3C$/N–C.

The surface functional groups on $Fe_3C$/N–C were investigated based on the Fourier transform infrared (FTIR) (Fig. 2B). The 3448 $cm^{-1}$ and 605 $cm^{-1}$ regions are ascribed to O–H or N–H stretching vibration and Fe–C stretch of $Fe_3C$, respectively [37,38]. The absorption band at 1619 $cm^{-1}$ and 1583 $cm^{-1}$ were caused by the vibrations of C=C and C=N bonds, respectively [39]. The presence of the band at 1334 $cm^{-1}$ is the characteristic of the C–H deformation vibration [40]. The C–O–C and C–O bonds are in the range of 1050 $cm^{-1}$ to 1250 $cm^{-1}$ [41,42]. The existence of Fe–C bonds at 587 $cm^{-1}$ further proves the possibility of the existence of $Fe_3C$. The graphitization of graphite-2H sheets has been confirmed by the Raman spectroscopy measurement. The Raman spectrum of $Fe_3C$/N–C was shown in Fig. 2C. Two typical peaks of 1353 $cm^{-1}$ and 1581 $cm^{-1}$ could be attributed to the D and G bands of graphite-2H, respectively [22,43,44]. The D and G bands in Raman spectra provide information about the defect density and crystallinity of $sp^2$ carbon [21]. The intensity ratio of the D/G value for the $Fe_3C$/N–C is 0.8, which indicates a high degree of graphitization. The graphite carbon structure can significantly enhance the conductivity of the products, thus can be used as the matrix for improving the biomimetic catalytic efficiency.

X-ray photoelectron spectroscopy (XPS) characterizations were carried out to further understand the composition and valence states of $Fe_3C$/N–C. The XPS survey spectrum exhibits the signals of Fe, O, N and C elements at 711, 532, 399, 284 eV (Fig. S7). The C 1s spectra could be deconvoluted into four peaks with corresponding binding energies to be 283.6 eV, 284.5 eV, 285.9 eV and 288.4 eV, which are in accordance with the C–Fe, C–C/C=C, C–N and C=O, respectively (Fig. 2D) [45–48]. The high-resolution Fe 2p XPS spectrum shows characteristic peaks of Fe $2p_{3/2}$ and Fe $2p_{1/2}$ peaks, respectively, confirming the existence of Fe (II) and, or Fe (III) state (Fig. 2E) [39]. Meanwhile, the peak at 708 eV was ascribed to the $Fe_3C$ [39]. The N 1s spectrum of the obtained $Fe_3C$/N–C can be deconvoluted into four peaks corresponding to pyridinic N (398.6 eV), pyrrolic N (399.8 eV), graphitic N (401.3 eV), and oxidized N (403.8 eV), respectively (Fig. S8) [18]. The XPS results were further indicative of the successful generation of the $Fe_3C$/N–C.

### 3.2. Kinetic studies and mechanism of $Fe_3C$/N–C about peroxidase-like activity

To explore the peroxidase (POD)-like activity of the $Fe_3C$/N–C, its catalytic oxidation of the chromogenic substrate TMB was carried out in the presence of $H_2O_2$. Catalytic oxidation of $Fe_3C$/N–C was monitored by the wavelength scanning mode to measure the corresponding catalytic activity. As can be seen in Fig. 3A, the TMB solution within the $H_2O_2$ or $Fe_3C$/N–C alone didn't show any UV–vis adsorption and the system is colourless (curves and inset a, b in Fig. 3A). In addition, there was no absorption peak for the $Fe_3C$/N–C containing the $H_2O_2$ alone in the NaAc-HAc buffer (pH 4.0) and the system was also colourless. (curve and inset c in Fig. 3A). All of these phenomena indicate that the oxidation reaction did not occur. However, when the TMB solution was added with both $H_2O_2$ and $Fe_3C$/N–C, the colour varied from colourless to blue (curve and inset d in Fig. 3A). It indicates that the $Fe_3C$/N–C could decompose $H_2O_2$ into •OH, which could lead to the oxidation of TMB to blue TMB oxides (ox-TMB) with maximum absorption peaks at 652 nm. The TA based fluorescence probe method was used to track the generated •OH, since the non-fluorescent TA can capture •OH to become TAOH with a fluorescence emission peak at 425 nm [49,50]. After 12 h of reaction, the fluorescence intensity of the mixture of TA within $H_2O_2$ was lower than that of TA within $H_2O_2$ and $Fe_3C$/N–C, which indicated the generation of •OH of the TA with $H_2O_2$ system due to the presence of $Fe_3C$/N–C (Fig. 3B). Besides, no fluorescence was observed when the TA was incubated with $Fe_3C$/N–C or TA alone. The ΔFL intensity (ΔCounts, Fig. S9) was also given to illustrate the sharp increase of the fluorescence intensity upon the addition of the catalyst, indicating the high catalysis efficiency of the $Fe_3C$/N–C. ESR was further carried out to detect the generation of •OH [7]. As shown in Fig. 3C, compared with the ESR signs for DMPO with only $H_2O_2$, the samples of DMPO with $Fe_3C$/N–C and $H_2O_2$ showed signs with intensity ratio of 1: 2: 2: 1 quartet format, further indicating the presence of •OH.

To verify whether the POD-like enzyme activity of $Fe_3C$/N–C comes from $Fe_3C$ or graphite-2H, the control experiments were conducted. The products of control **6** and **7** have been characterized by XRD or FTIR as shown in Fig. S10 and Fig. S11 in the Supporting Information, respectively. As shown, the POD-like activity can also be observed for the graphite-2H without $Fe_3C$ obtained by control experiment **6** (Fig. S10 and curve e in Fig. 3A), or N-doped graphitic carbon (N–C) by control experiment **7** (Fig. S11 and curve f in Fig. 3A), respectively. The N–C in control **7** could endow higher catalytic activity than control **6**, confirming the positive effects of N doping on the enzyme-like activity of the as-prepared nanomaterials. However, all the two absorption peak intensities were much relatively lower than that of $Fe_3C$/N–C. It was further confirmed that the POD-like activity was mainly resulted from the $Fe_3C$. While the N doping into the carbon matrices could further enhance the catalytic activity of the graphite-2H [12,13]. Accordingly, the synergistic effect between $Fe_3C$ and N-graphite-2H can

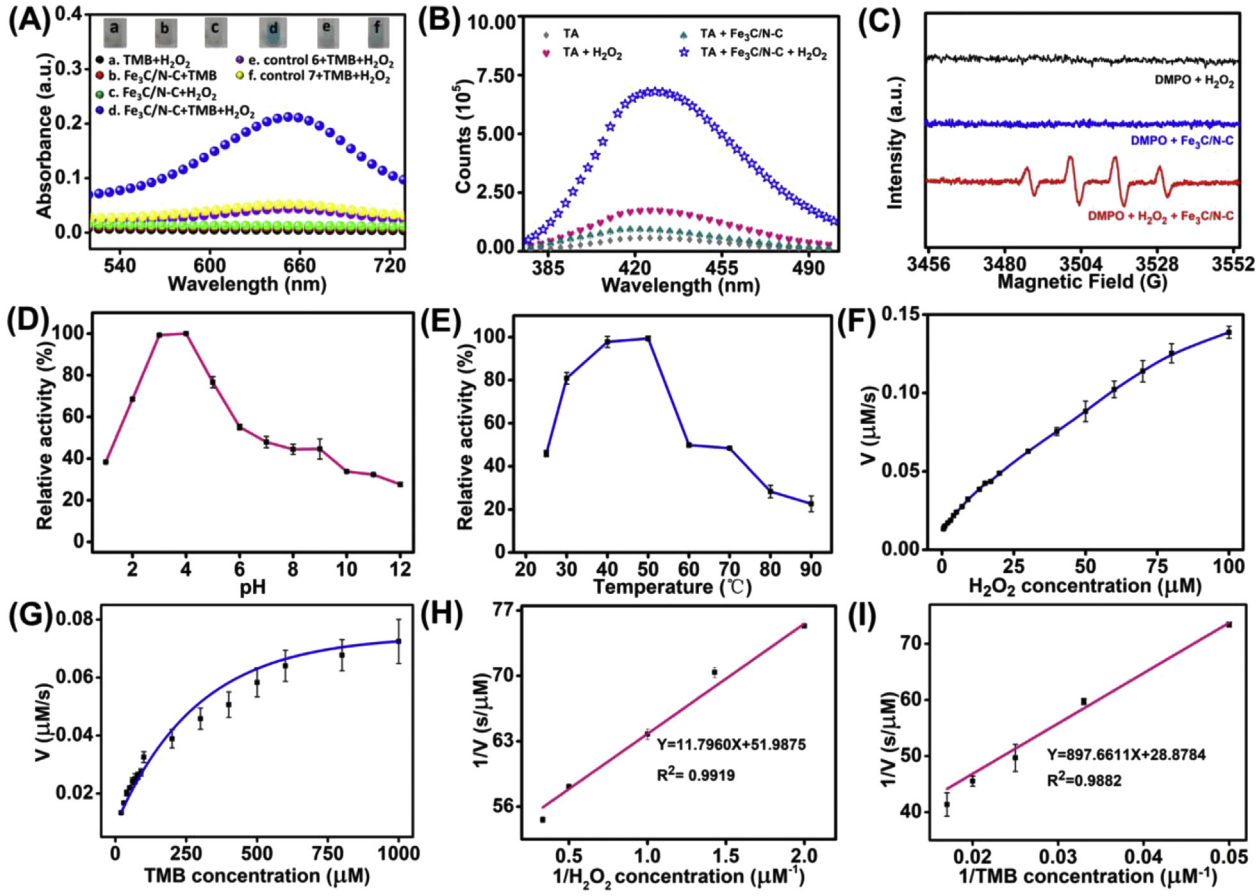


**Fig. 3.** (A) The absorbance spectra in different reaction systems in the NaAc-HAc buffer (pH 4.0) at 25 °C after 5 min incubation. (B) The fluorescence spectra of TAOH formed under different conditions. (C) ESR spectra of DMPO-OH. The dependence of the peroxidase-like catalytic activity of the $Fe_3C$/N–C on the pH (D) and temperature (E). Steady-state kinetic assay and double-reciprocal plots of the $Fe_3C$/N–C. (F) The concentration of the TMB was 0.5 mM, and the $H_2O_2$ concentration was ranging from 0.5 to 100 μM. (G) The concentration of $H_2O_2$ was 100 μM and the TMB concentration changed from 20 μM to 1 mM. (H) and (I) Double-reciprocal plots for the activity of $Fe_3C$/N–C at a fixed concentration of one substrate and the other varied. (A colour version of this figure can be viewed online.)

significantly improve the POD-like enzyme activity of $Fe_3C$/N–C [51–53].

As shown in Fig. 3, we studied the influence of pH (Fig. 3D) and temperature (Fig. 3E) on the peroxidase-like catalytic activity of $Fe_3C$/N–C. Compared with the HRP, $Fe_3C$/N–C exhibited excellent catalytic activity in a wide range of pH (1.0–11.0) and temperature (25–70 °C) [54]. The optimum reaction conditions for $Fe_3C$/N–C were pH 4.0 and temperature 50 °C. Also, it had better pH tolerance than many peroxidase mimics such as $Fe_3O_4$ NPs [55], graphene oxide [56] and CNDs [57]. The peroxidase-like activity of $Fe_3C$/N–C was further studied based on the steady-state kinetics. Apparent kinetics data were obtained by changing the concentration of TMB or $H_2O_2$ while maintaining the other concentration unchanged. The typical Michaelis–Menten curves were observed for $Fe_3C$/N–C (Fig. 3F and G). Kinetic parameters $K_m$ and $V_{max}$ were obtained by fitting the Michaelis-Menten model and Lineweaver-Burk equation (Fig. 3H and I) [58], which are listed in Table S1. The results showed that the redox reaction catalyzed by $Fe_3C$/N–C followed the typical Michaelis-Menten behaviour towards the two substrates of TMB and $H_2O_2$ [59,60]. Comparisons with other peroxidase-like nanomaterials such as $Fe_3O_4$ NPs, $MoS_2$, Au/$Co_3O_4$-CeOx NCs and $WSe_2$ nanosheets were shown in Table S2. The $Fe_3C$/N–C possessed lower $K_m$ value for both TMB and $H_2O_2$, suggesting the higher affinity of $Fe_3C$/N–C with the substrates, respectively. It also showed superior or comparable $V_{max}$ value. *i.e.* catalytic efficiency to many previous nanozymes [55,58,61,62].

### 3.3. Cytotoxicity measurement

As reported, nanomaterials with peroxidase-like properties should have promising application potentials in bio-applications. Thus the biocompatibility should be a criterion for evaluating their feasibility both *in vitro* and *in vivo* applications. Accordingly, the MTT assay was performed to investigate the cytotoxicity of the $Fe_3C$/N–C on the HeLa cells at different concentration ranging from 0 to 300 μg $mL^{-1}$ after 4 h and 24 h treatment, respectively. As shown in Fig. S12, taking the one without $Fe_3C$/N–C culture as 100%, all cells survival rate can reach about 80%, even in the

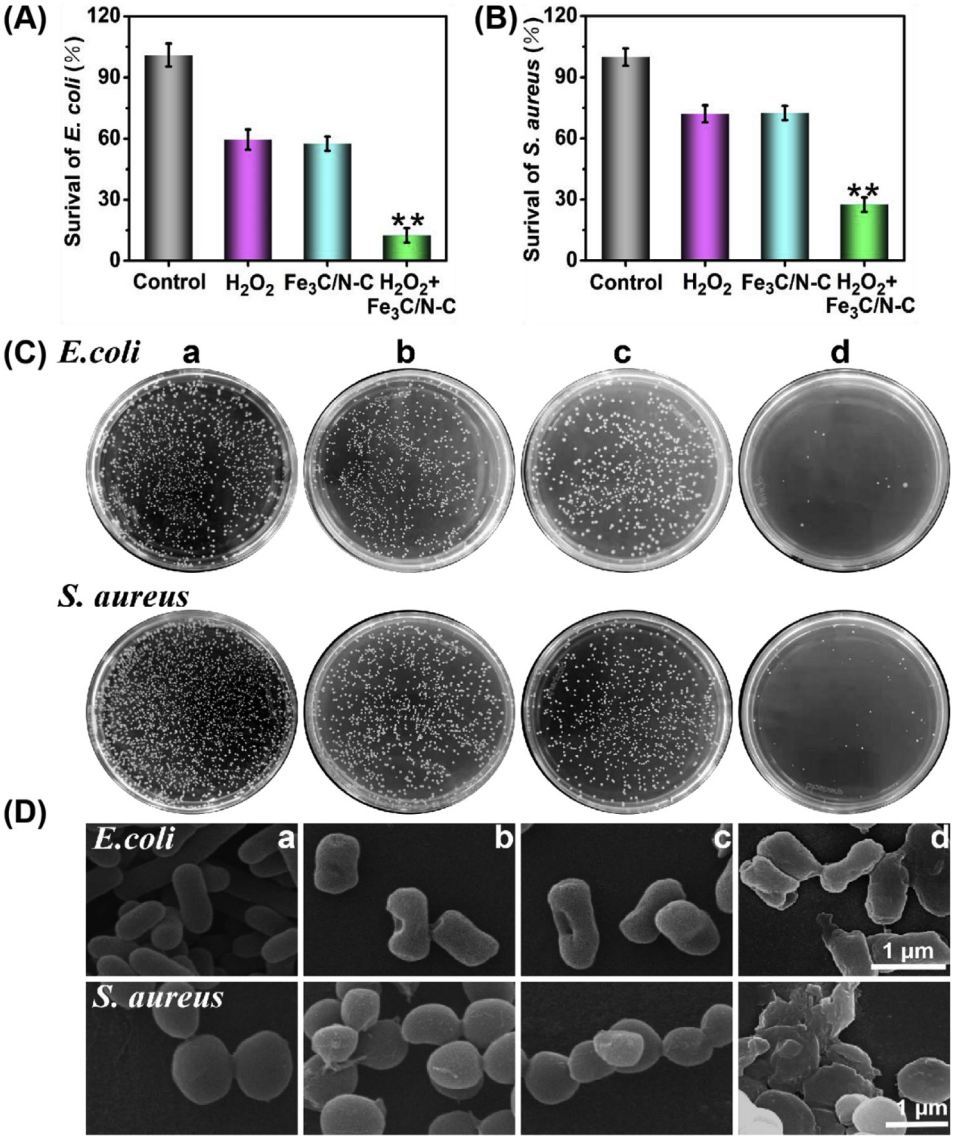


**Fig. 4.** The characterizations of *E. coli* and *S. aureus* upon various treatments by CFU method: The survival rates of (A) *E. coli* and (B) *S. aureus*. (C) The representative photograph of bacterial colonies. (D) The typical SEM images. (a) PBS as control, (b) $H_2O_2$ (1 mM), (c) $Fe_3C$/N–C (100 μg $mL^{-1}$) and (d) $H_2O_2$ + $Fe_3C$/N–C, respectively. The error bars stand for the standard deviation (n = 3). Asterisks represent statistically significant differences (**$p < 0.01$). (A colour version of this figure can be viewed online.)

presence of $Fe_3C$/N–C at high concentration of 300 μg $mL^{-1}$. As a result, the excellent biocompatibility of the as-obtained $Fe_3C$/N–C to the cells can be confirmed by the MTT assay.

### 3.4. Applications

#### 3.4.1. Antibacterial activity of $Fe_3C$/N–C

It was known that $H_2O_2$ had been popularly applied in treating bacterial infections. However, compared to $H_2O_2$, the •OH exhibited stronger oxidizing properties and eletrophilicity, which could lead to more lipids or amino acids to be damaged and kill bacterial more efficacious [63]. Due to its excellent peroxidase activity that could catalyze $H_2O_2$ to generate •OH. Therefore, the as-prepared $Fe_3C$/N–C was highly expected to improve the antibacterial ability of $H_2O_2$.

To evaluate the antibacterial activity of $Fe_3C$/N–C, the bacterial survival rate was studied taking *E. coli* and *S. aureus* as the Gram-negative and Gram-positive bacteria examples, respectively. As indicated in Fig. 4A–B, after treatment with PBS, $H_2O_2$, $Fe_3C$/N–C or $H_2O_2$ + $Fe_3C$/N–C, there was a noticeable phenomenon that the bacterial survival rate in $H_2O_2$ + $Fe_3C$/N–C group was significantly lower than other control groups. These results suggested that the $Fe_3C$/N–C had excellent antibacterial activity in the presence of $H_2O_2$, which could be potentially due to the production of •OH via the peroxidase reaction of $Fe_3C$/N–C within $H_2O_2$. Besides, Fig. 4C showed the bacterial colonies on solid medium, which was more intuitive to exhibit the changes in the number of bacterial colonies. As expected, bacterial colonies were hardly observed in $H_2O_2$ + $Fe_3C$/N–C group. Furthermore, the dose-dependent antibacterial manner of $H_2O_2$ in the absence and presence of the $Fe_3C$/N–C was evaluated. As shown in Fig. S13, the concentration of $H_2O_2$ within the $Fe_3C$/N–C could be decreased to 10–100 folds with the assistance of $Fe_3C$/N–C to reach the comparable antibacterial efficiency of $H_2O_2$ alone.

SEM was utilized to characterize the cell morphology variations before and after treatment. As shown in Fig. 4D, the untreated *E. coli* or *S. aureus* cells exhibited rod- and spherical-like shapes, respectively. After treatment with $H_2O_2$ or $Fe_3C$/N–C, both the cell wall of *E. coli* and *S. aureus* cell turned from smooth and intact to slightly rough and wrinkled. Notably, the bacterial cells were observed to be relatively more severely rough and damaged in the presence of $Fe_3C$/N–C + $H_2O_2$ group. These results were corresponded to the CFU method, suggesting that $H_2O_2$ with the assistance of $Fe_3C$/N–C have more excellent antibacterial activity against both *E. coli* and *S. aureus*.

To further explore the bacterial cell wall integrity after treatment, fluorescence-based Live/Dead assays were performed taking *E. coli* as an example. There were only a few red spots to be observed in the control group (Fig. 5), indicating most bacteria were still alive. The bacterial group treated with $H_2O_2$ or $Fe_3C$/N–C alone showed a little redder fluorescent cells. While in the presence of both $Fe_3C$/N–C + $H_2O_2$, a large number of red fluorescent cells were

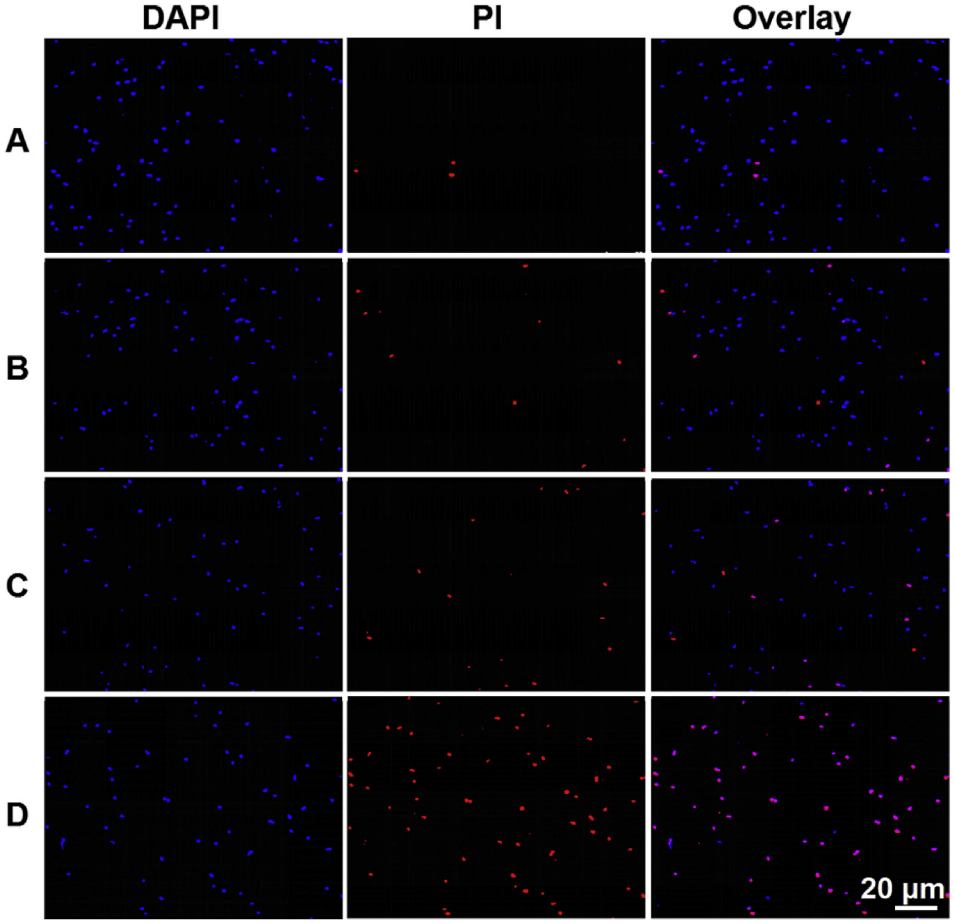


**Fig. 5.** Fluorescence images of live and dead *E. coli* cells treated with (A) PBS as control, (B) $H_2O_2$ (1 mM), (C) $Fe_3C$/N–C (100 μg $mL^{-1}$) or (D) $H_2O_2$ + $Fe_3C$/N–C. Both the cell nucleus of live and dead cells could be stained by DAPI with blue fluorescence, while the PI could only be used to stain the dead cells with red fluorescence. Bar scale: 20 μm. (A colour version of this figure can be viewed online.)

observed, implying that the cell wall of *E. coli* was severely damaged. All the results above were in accordance with the SEM data and spread plate assays, again demonstrating the increased antibacterial activity of $H_2O_2$ with the assistance of the as-prepared $Fe_3C$/N–C.

### 3.4.2. Wound infection treated by $Fe_3C$/N–C

To verify the feasibility of antibacterial properties of $H_2O_2$ + $Fe_3C$/N–C in wound healing, *in-vivo* tests were carried out by Sprague–Dawley (SD) rats with the wound on their back. *S. aureus* cells of $10^6$ CFU $mL^{-1}$ were induced to a bacterial infection on the wound. It has been reported that $H_2O_2$ with the high concentration of 0.1 M–1.0 M, was harmful to the healthy tissues and finally slow down the rate of wound healing [64], while low concentration of $H_2O_2$ was more conducive for optimal healing. Herein, with the assistance of $Fe_3C$/N–C, only 1 mM $H_2O_2$ was applied for synergistic antibacterial treatment, which was much lower than the usual amount [5]. As shown in Fig. 6A, four groups of rats were treated with PBS, $H_2O_2$ (1 mM), $Fe_3C$/N–C (100 μg $mL^{-1}$), $H_2O_2$ (1 mM) + $Fe_3C$/N–C (100 μg $mL^{-1}$), respectively. Compared with other groups, the $H_2O_2$ + $Fe_3C$/N–C group exhibited significant wound healing and skin regeneration ability, which was almost completely healed after 6 days. Furthermore, the wound area was quantified via comparing wound size in different periods (2, 4 and 6 days, respectively) with wound size on day 0. It could be observed from Fig. 6B that the group treated with $H_2O_2$ + $Fe_3C$/N–C could effectively accelerate wound healing as compared with other groups. In addition, *S. aureus* cells collected from wound tissue were used to evaluate the antimicrobial efficacy of different treatments by CFU method. As indicated in Fig. 6C, the $H_2O_2$ + $Fe_3C$/N–C group exhibited much fewer bacterial colonies than other control groups. The enhanced wound healing was resulted from the antibacterial effects of the $H_2O_2$ + $Fe_3C$/N–C system. Meanwhile, the healing process was assessed by using the H&E staining method. In Fig. 6D, the histological analyses revealed that the group treated with both $H_2O_2$ + $Fe_3C$/N–C exhibited intact and thickened epidermis, while there was still visible fragmentary epidermal layers can be seen in other control groups. Furthermore, with the assistance of both $H_2O_2$ and $Fe_3C$/N–C, hair follicles and the blood vessels recovered quickly than other control groups.

### 3.4.3. Biosafety of $Fe_3C$/N–C

To further study the *in vivo* biosafety of $Fe_3C$/N–C, the as-prepared $Fe_3C$/N–C was injected intravenously into healthy rats [30]. Blood physiological index was tested to study the liver and kidney function after the sixth day of the experiment. As shown in Fig. 7A, there were no apparent differences in these indicators being found upon the comparison with the untreated rats. Furthermore, the major organs (liver, spleen, heart, lung and kidney) were harvested and stained with H&E. As expected, no apparent organ abnormality or inflammation was observed in Fig. 7B. All of the above results demonstrated the as-prepared $Fe_3C$/N–C had proper biosafety with low cytotoxicity, which was an ideal nanomaterial for antibacterial and wound healing *in vivo*.

## 4. Conclusion

The $Fe_3C$/N-doped graphitic carbon nanomaterials ($Fe_3C$/N–C) were prepared through a one-step mild electrochemical method herein, avoiding high-temperature carbonization and time-consumption preparation process. The $Fe_3C$/N–C possessed excellent biocompatibility, high peroxidase-like catalytic activity and cost-effectiveness simultaneously. The generation of $Fe_3C$/N–C was ingeniously benefiting from the specific affinity interactions between the His derived CNDs and the iron ion, which is a distinct application of this affinity since it was only used for sensing

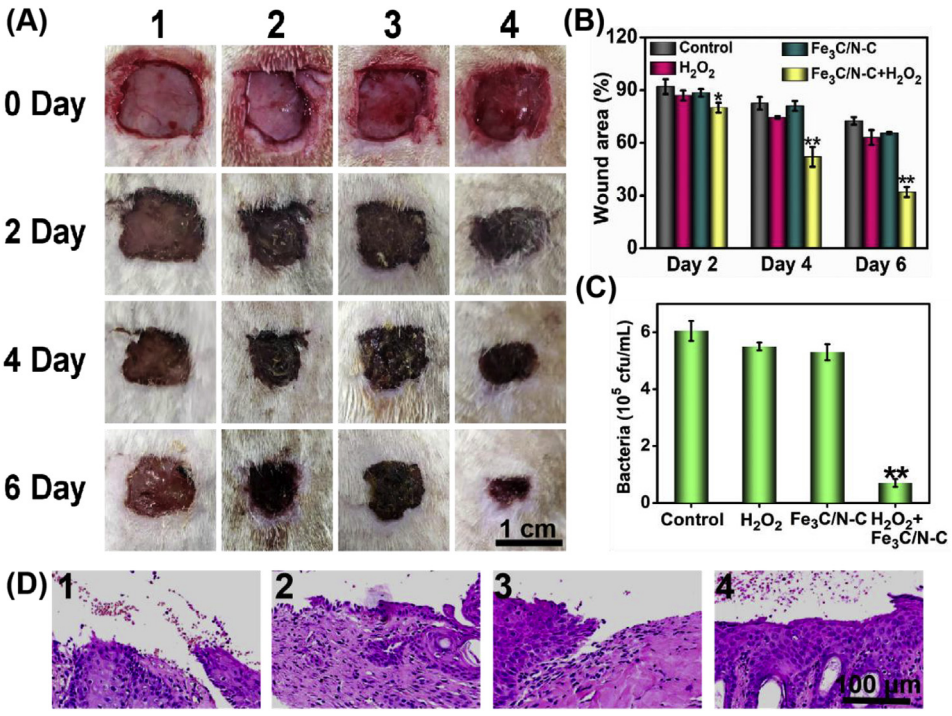


**Fig. 6.** *In vivo* wound healing experiment treated with (1) PBS, (2) $H_2O_2$ (1 mM), (3) $Fe_3C$/N–C (100 μg $mL^{-1}$), or (4) $H_2O_2$ (1 mM) + $Fe_3C$/N–C (100 μg $mL^{-1}$). (A) Photographs of wound on rat back from the four groups. (B) The wound area in different periods (2, 4 and 6 days). (C) The number of bacterial colonies was quantified by the CFU method after the sixth day of the experiment. (D) Histological data of wound tissues after different treatments. Error bars stand for the standard deviation (n = 3). Asterisks were the statistically significant differences ($^*p < 0.05$, $^{**}p < 0.01$). (A colour version of this figure can be viewed online.)

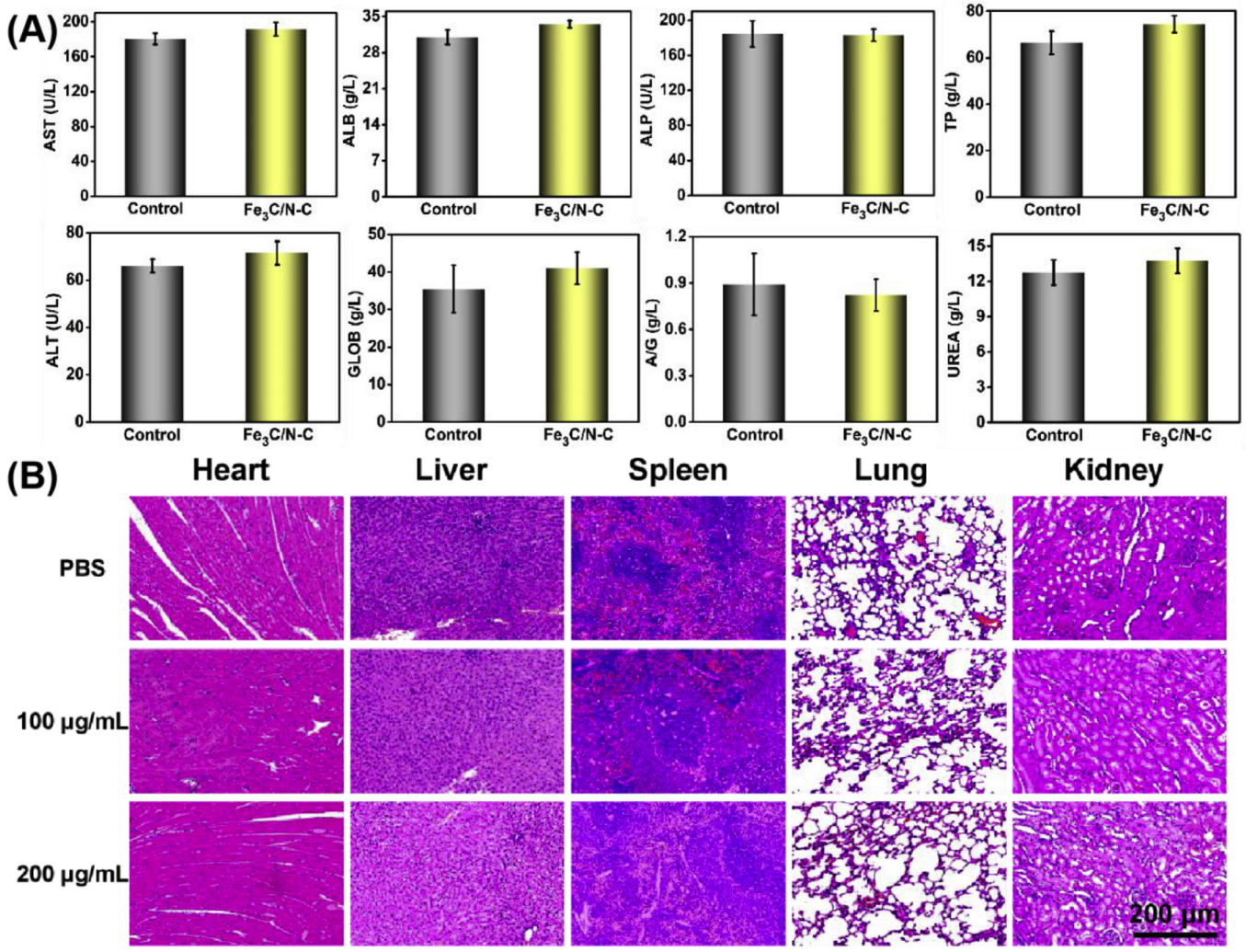


**Fig. 7.** (A) Blood biochemistry data including aspartate transaminase (AST), albumin (ALB), alkaline phosphatase (ALP), total protein (TP), alanine transaminase (ALT), globulin (GLOB), the ratio of albumin and globulin (A/G) and urea nitrogen (UREA). (B) H&E staining measurement of the main organs treated with different concentration of $Fe_3C$/N–C or PBS as control. (A colour version of this figure can be viewed online.)

applications before. The $Fe_3C$/N–C nanozyme showed excellent broad-spectrum antimicrobial activity, which could endow efficient antibacterial treatment of wound infection *in vivo* even in the presence of much lower-concentration of $H_2O_2$ (1.0 mM). The superior peroxidase-like ability can be attributed to the $Fe_3C$ active site and the synergistic interface effect between $Fe_3C$ and N-doped graphite carbon matrix. The work not provides simple ways for $Fe_3C$ based nanomaterials but also opens the enzyme-like study of $Fe_3C$. All these efforts will bring advances in nanotechnology, biomedical and enzyme catalysis study.

## Declaration of competing interestCOI

The authors declare no competing financial interest.

## CRediT author statement

**Yang Li:** Conceptualization, Methodology, Validation, Formal analysis, Investigation, Data Curation, Writing - Original Draft, Writing - Review & Editing **Weishuai Ma:** Writing - Original Draft, Writing - Review & Editing **Jing Sun:** Resources **Min Lin:** Investigation **Yusheng Niu:** Project administration **Xuecheng Yang:** Resources **Yuanhong Xu:** Conceptualization, Methodology, Project administration

## Acknowledgements

This work was supported by the National Natural Science Foundation of China (No. 21874079), Natural Science Foundation for Outstanding Young Scientists of Shandong Province (ZR2018JL011), Key R&D Project of Shandong Province (GG201809230180), Qingdao Science & Technology Planning Project (17-6-3-15-gx), and Science & Technology Fund Planning Project of Shandong Colleges and Universities (J16LA13 & J18KA112).

## Appendix A. Supplementary data

Supplementary data to this article can be found online at https://doi.org/10.1016/j.carbon.2019.11.093.

## References

[1] S.R. Ali, S. Pandit, M. De, 2D-$MoS_2$-based β-Lactamase inhibitor for combination therapy against drug-resistant bacteria, ACS Appl. Bio Mater. 1 (2018) 967–974.

[2] Y. Hou, Q. Lu, J. Deng, H. Li, Y. Zhang, One-pot electrochemical synthesis of functionalized fluorescent carbon dots and their selective sensing for mercury ion, Anal. Chim. Acta 866 (2015) 69–74.

[3] C. Zhu, H. Li, H. Wang, B. Yao, H. Huang, Y. Liu, et al., Negatively charged carbon nanodots with bacteria resistance ability for high-performance antibiofilm formation and anticorrosion coating design, Small 15 (2019) 1900007.

[4] J. Wu, X. Wang, Q. Wang, Z. Lou, S. Li, Y. Zhu, et al., Nanomaterials with enzyme-like characteristics (nanozymes): next-generation artificial enzymes (II), Chem. Soc. Rev. 48 (2019) 1004–1076.

[5] H. Sun, N. Gao, K. Dong, J. Ren, X. Qu, Graphene quantum dots-band-aids used for wound disinfection, ACS Nano 8 (2014) 6202–6210.

[6] Y. Tao, E. Ju, J. Ren, X. Qu, Bifunctionalized mesoporous silica-supported gold nanoparticles: intrinsic oxidase and peroxidase catalytic activities for antibacterial applications, Adv. Mater. 27 (2015) 1097–1104.

[7] C. Ge, R. Wu, Y. Chong, G. Fang, X. Jiang, Y. Pan, et al., Synthesis of Pt hollow nanodendrites with enhanced peroxidase-like activity against bacterial infections: implication for wound healing, Adv. Funct. Mater. 28 (2018) 1801484.

[8] L. Gao, K.M. Giglio, J.L. Nelson, H. Sondermann, A.J. Travis, Ferromagnetic nanoparticles with peroxidase-like activity enhance the cleavage of biological macromolecules for biofilm elimination, Nanoscale 6 (2014) 2588–2593.

[9] F. Natalio, R. André, A.F. Hartog, B. Stoll, K.P. Jochum, R. Wever, et al., Vanadium pentoxide nanoparticles mimic vanadium haloperoxidases and thwart biofilm formation, Nat. Nanotechnol. 7 (2012) 530–535.

[10] Y. Zhao, J. Zhang, X. Guo, H. Fan, W. Wu, H. Liu, et al., $Fe_3C$@nitrogen doped CNT arrays aligned on nitrogen functionalized carbon nanofibers as highly efficient catalysts for the oxygen evolution reaction, J. Mater. Chem. A 5 (2017) 19672–19679.

[11] N. Song, F. Ma, Y. Zhu, S. Chen, C. Wang, X. Lu, $Fe_3C$/nitrogen-doped carbon nanofibers as highly efficient biocatalyst with oxidase-mimicking activity for colorimetric sensing, ACS Sustain. Chem. Eng. 6 (2018) 16766–16776.

[12] M.Y. Emran, M.A. Shenashen, H. Morita, S.A. El-Safty, One-step selective screening of bioactive molecules in living cells using sulfur-doped microporous carbon, Biosens. Bioelectron. 109 (2018) 237–245.

[13] Y. Emran Mohammed, M. Mekawy, N. Akhtar, A. Shenashen Mohamed, M. El-Sewify Islam, A. Faheem, et al., Broccoli-shaped biosensor hierarchy for electrochemical screening of noradrenaline in living cells, Biosens. Bioelectron. 100 (2018) 122–131.

[14] A. Aijaz, J. Masa, C. Rösler, H. Antoni, R.A. Fischer, W. Schuhmann, et al., MOF-templated assembly approach for $Fe_3C$ nanoparticles encapsulated in bamboo-like N-doped CNTs: highly efficient oxygen reduction under acidic and basic conditions, Chem. Eur J. 23 (2017) 12125–12130.

[15] Y. Liao, K. Pan, L. Wang, Q. Pan, W. Zhou, X. Miao, et al., Facile synthesis of high-crystallinity graphitic carbon/$Fe_3C$ nanocomposites as counter electrodes for high-efficiency dye-sensitized solar cells, ACS Appl. Mater. Interfaces 5 (2013) 3663–3670.

[16] H. Yuan, X. Zhang, F. Yan, S. Zhang, C. Zhu, C. Li, et al., Nitrogen-doped carbon nanosheets containing $Fe_3C$ nanoparticles encapsulated in nitrogen-doped graphene shells for high-performance electromagnetic wave absorbing materials, Carbon 140 (2018) 368–376.

[17] J. Ju, M. Kim, S. Jang, Y. Kim, Y. Choi, S.-H. Baeck, et al., 3D in-situ hollow carbon fiber/carbon nanosheet/$Fe_3C$@$Fe_3O_4$ by solventless one-step synthesis and its superior supercapacitor performance, Electrochim. Acta 252 (2017) 215–225.

[18] H. Yang, J. Xiao, L. Su, T. Feng, Q. Lv, X. Zhang, Oxidase-mimicking activity of the nitrogen-doped $Fe_3C$@C composites, Chem. Commun. 53 (2017) 3882–3885.

[19] N. Song, F. Ma, Y. Zhu, S. Chen, C. Wang, X. Lu, $Fe_3C$/nitrogen-doped carbon nanofibers as highly efficient biocatalyst with oxidase-mimicking activity for colorimetric sensing, ACS Sustain. Chem. Eng. 6 (2018) 16766–16776.

[20] L. Su, Z. Zhou, P. Shen, Core–shell Fe@$Fe_3C$/C nanocomposites as anode materials for Li ion batteries, Electrochim. Acta 87 (2013) 180–185.

[21] A.A. Dimiev, K. Shukhina, N. Behabtu, M. Pasquali, J.M. Tour, Stage transitions in graphite intercalation compounds: role of the graphite structure, J. Phys. Chem. C 123 (2019) 19246–19253.

[22] R. Nandan, K.K. Nanda, Designing N-doped carbon nanotubes and Fe–$Fe_3C$ nanostructures co-embedded in B-doped mesoporous carbon as an enduring cathode electrocatalyst for metal–air batteries, J. Mater. Chem. A 5 (2017) 16843–16853.

[23] M. Liu, Y. Xu, F. Niu, J.J. Gooding, J. Liu, Carbon quantum dots directly generated from electrochemical oxidation of graphite electrodes in alkaline alcohols and the applications for specific ferric ion detection and cell imaging, Analyst 141 (2016) 2657–2664.

[24] F. Niu, Y. Xu, M. Liu, J. Sun, P. Guo, J. Liu, Bottom-up electrochemical preparation of solid-state carbon nanodots directly from nitriles/ionic liquids using carbon-free electrodes and the applications in specific ferric ion detection and cell imaging, Nanoscale 8 (2016) 5470–5477.

[25] F. Niu, Y. Xu, J. Liu, Z. Song, M. Liu, J. Liu, Controllable electrochemical/electroanalytical approach to generate nitrogen-doped carbon quantum dots from varied amino acids: pinpointing the utmost quantum yield and the versatile photoluminescent and electrochemiluminescent applications, Electrochim. Acta 236 (2017) 239–251.

[26] F. Liu, F. Niu, T. Chen, J. Han, Z. Liu, W. Yang, et al., One-step electrochemical strategy for in-situ synthesis of S, N-codoped graphene as metal-free catalyst for oxygen reduction reaction, Carbon 134 (2018) 316–325.

[27] A. Ejigu, B. Miller, I.A. Kinloch, R.A.W. Dryfe, Optimisation of electrolytic solvents for simultaneous electrochemical exfoliation and functionalisation of graphene with metal nanostructures, Carbon 128 (2018) 257–266.

[28] K. Parvez, Z.-S. Wu, R. Li, X. Liu, R. Graf, X. Feng, et al., Exfoliation of graphite into graphene in aqueous solutions of inorganic salts, J. Am. Chem. Soc. 136 (2014) 6083–6091.

[29] Z. Chen, X. Gao, X. Wei, X. Wang, Y. Li, T. Wu, et al., Directly anchoring $Fe_3C$ nanoclusters and FeNx sites in ordered mesoporous nitrogen-doped graphitic carbons to boost electrocatalytic oxygen reduction, Carbon 121 (2017) 143–153.

[30] Y. Wang, X. Ding, Y. Chen, M. Guo, Y. Zhang, X. Guo, et al., Antibiotic-loaded, silver core-embedded mesoporous silica nanovehicles as a synergistic antibacterial agent for the treatment of drug-resistant infections, Biomaterials 101 (2016) 207–216.

[31] M. Ming, S. You, W. Wang, G. Liu, D. Qi, X. Chen, et al., Biomass–derived porous $Fe_3C$/WC/GC nanocomposite for efficient electrocatalysis of oxygen reduction, ACS Appl. Mater. Interfaces 8 (2016) 32307–32316.

[32] W. Yang, X. Liu, X. Yue, J. Jia, S. Guo, Bamboo-like carbon nanotube/$Fe_3C$ nanoparticle hybrids and their highly efficient catalysis for oxygen reduction, J. Am. Chem. Soc. 137 (2015) 1436–1439.

[33] H. Liu, Y. Li, M. Yuan, G. Sun, Q. Liao, Y. Zhang, Solid and macroporous $Fe_3C$/N-C nanofibers with enhanced electromagnetic wave absorbability, Sci. Rep. 8 (2018) 16832.

[34] J. Deng, Q. Lu, N. Mi, H. Li, M. Liu, M. Xu, et al., Electrochemical synthesis of carbon nanodots directly from alcohols, Chem. Eur J. 20 (2014) 4993–4999.

[35] D.G. Marangoni, R.S. Smith, S.G. Roscoe, Surface electrochemistry of the oxidation of glycine at Pt, Can. J. Chem. 67 (1989) 921–926.

[36] C. Wang, W. Wu, A.P. Periasamy, H. Chang, Electrochemical synthesis of photoluminescent carbon nanodots from glycine for highly sensitive detection of hemoglobin, Green Chem. 16 (2014) 2509–2514.

[37] M.M. Mian, G. Liu, Sewage sludge-derived $TiO_2$/Fe/$Fe_3C$-biochar composite as an efficient heterogeneous catalyst for degradation of methylene blue, Chemosphere 215 (2019) 101–114.

[38] J. Li, S. Yang, Y. Deng, P. Chai, Y. Yang, X. He, et al., Emancipating target-functionalized carbon dots from autophagy vesicles for a novel visualized tumor therapy, Adv. Funct. Mater. 28 (2018) 1800881.

[39] F. Kong, X. Fan, A. Kong, Z. Zhou, X. Zhang, Y. Shan, Covalent phenanthroline framework derived FeS@$Fe_3C$ composite nanoparticles embedding in n-s-codoped carbons as highly efficient trifunctional electrocatalysts, Adv. Funct. Mater. 28 (2018) 1803973.

[40] X. Wang, P. Zhang, W. Wang, X. Lei, H. Yang, Magnetic N-enriched $Fe_3C$/graphitic carbon instead of Pt as an electrocatalyst for the oxygen reduction reaction, Chem. Eur J. 22 (2016) 4863–4869.

[41] X. Bai, X. Zhang, Z. Hua, W. Ma, Z. Dai, X. Huang, et al., Uniformly distributed anatase $TiO_2$ nanoparticles on graphene: synthesis, characterization, and photocatalytic application, J. Alloy. Comp. 599 (2014) 10–18.

[42] Y. Si, E.T. Samulski, Synthesis of water soluble graphene, Nano Lett. 8 (2008) 1679–1682.

[43] Y. Wang, G. Zhang, G. Liu, W. Liu, H. Chen, J. Yang, Facile synthesis of highly porous N-doped CNTs/$Fe_3C$ and its electrochemical properties, RSC Adv. 6 (2016) 44013–44018.

[44] J. Yang, J. Hu, M. Weng, R. Tan, L. Tian, J. Yang, et al., Fe-cluster pushing electrons to N-doped graphitic layers with $Fe_3C$(Fe) hybrid nanostructure to enhance $O_2$ reduction catalysis of Zn-air batteries, ACS Appl. Mater. Interfaces 9 (2017) 4587–4596.

[45] C. Wei, M. Shen, K. Ai, L. Lu, Transformation from FeS/$Fe_3C$ nanoparticles encased S, N dual doped carbon nanotubes to nanosheets for enhanced oxygen reduction performance, Carbon 123 (2017) 135–144.

[46] M. Zou, L. Wang, J. Li, L. Guan, Z. Huang, Enhanced Li-ion battery performances of yolk-shell $Fe_3O_4$@C anodes with $Fe_3C$ catalyst, Electrochim. Acta 233 (2017) 85–91.

[47] J. Dai, S. Tian, Y. Jiang, Z. Chang, A. Xie, R. Zhang, et al., $Fe_3C$/Fe/C magnetic hierarchical porous carbon with micromesopores for highly efficient chloramphenicol adsorption: magnetization, graphitization, and adsorption properties investigation, Ind. Eng. Chem. Res. 57 (2018) 3510–3522.

[48] H. Li, W. Kong, J. Liu, N. Liu, H. Huang, Y. Liu, et al., Fluorescent N-doped carbon dots for both cellular imaging and highly-sensitive catechol detection, Carbon 91 (2015) 66–75.

[49] Y. Xing, X. Liu, Q. Pu, M. Wu, J.X. Zhao, Biocompatible G-quadruplex/hemin for enhancing antibacterial activity of $H_2O_2$, ACS Appl. Bio Mater. 1 (2018) 1019–1027.

[50] L. Huang, Y. Niu, R. Li, H. Liu, Y. Wang, G. Xu, et al., $VO_x$ quantum dots with multienzyme-mimic activities and the application in constructing a three-dimensional (3D) coordinate system for accurate discrimination of the hydrogen peroxide over a broad concentration range, Anal. Chem. 91 (2019) 5753–5761.

[51] M. Xiao, Y. Meng, C. Duan, F. Zhu, Y. Zhang, Ionic liquid derived $Co_3O_4$/Nitrogen doped carbon composite as anode of lithium ion batteries with enhanced rate performance and cycle stability, J. Mater. Sci. Mater. Electron. 30 (2019) 6148–6156.

[52] Z.R. Ismagilov, A.E. Shalagina, O.Y. Podyacheva, A.V. Ischenko, L.S. Kibis, A.I. Boronin, et al., Structure and electrical conductivity of nitrogen-doped carbon nanofibers, Carbon 47 (2009) 1922–1929.

[53] K. Xiao, Y. Liu, Pa Hu, G. Yu, Y. Sun, D. Zhu, n-Type field-effect transistors made of an individual nitrogen-doped multiwalled carbon nanotube, J. Am. Chem.

Soc. 127 (2005) 8614–8617.
[54] Vinita, N.R. Nirala, R. Prakash, One step synthesis of AuNPs@$MoS_2$-QDs composite as a robust peroxidase- mimetic for instant unaided eye detection of glucose in serum, saliva and tear, Sens. Actuators B Chem. 263 (2018) 109–119.
[55] G. Lizeng, Z. Jie, N. Leng, Z. Jinbin, Z. Yu, G. Ning, et al., Intrinsic peroxidase-like activity of ferromagnetic nanoparticles, Nat. Nanotechnol. 2 (2007) 577–583.
[56] Y. Song, K. Qu, C. Zhao, J. Ren, X. Qu, Graphene oxide: intrinsic peroxidase catalytic activity and its application to glucose detection, Adv. Mater. 22 (2010) 2206–2210.
[57] R.V. Gorbachev, I. Riaz, R.R. Nair, R. Jalil, L. Britnell, B.D. Belle, et al., Hunting for monolayer boron nitride: optical and Raman signatures, Small 7 (2011) 465–468.
[58] T. Lin, L. Zhong, L. Guo, F. Fu, G. Chen, Seeing diabetes: visual detection of glucose based on the intrinsic peroxidase-like activity of $MoS_2$ nanosheets, Nanoscale 6 (2014) 11856–11862.
[59] L. Ai, L. Li, C. Zhang, J. Fu, J. Jiang, MIL-53(Fe): a metal–organic framework with intrinsic peroxidase-like catalytic activity for colorimetric biosensing, Chem. Eur J. 19 (2013) 15105–15108.
[60] K. Cai, Z. Lv, K. Chen, L. Huang, J. Wang, F. Shao, et al., Aqueous synthesis of porous platinum nanotubes at room temperature and their intrinsic peroxidase-like activity, Chem. Commun. 49 (2013) 6024–6026.
[61] H. Liu, Y. Ding, B. Yang, Z. Liu, Q. Liu, X. Zhang, Colorimetric and ultrasensitive detection of $H_2O_2$ based on Au/$Co_3O_4$-$CeO_x$ nanocomposites with enhanced peroxidase-like performance, Sens. Actuators B Chem. 271 (2018) 336–345.
[62] T. Chen, X. Wu, J. Wang, G. Yang, $WSe_2$ few layers with enzyme mimic activity for high-sensitive and high-selective visual detection of glucose, Nanoscale 9 (2017) 11806–11813.
[63] J.M.C. Gutteridge, S. Wilkins, Copper-dependent hydroxyl radical damage to ascorbic acid, FEBS Lett. 137 (1982) 327–330.
[64] A.E.K. Loo, W. Yee Ting, H. Rongjian, W. Martin, D. Tiehua, N. Wee Thong, et al., Effects of hydrogen peroxide on wound healing in mice in relation to oxidative damage, PLoS One 7 (2012) 49215.